10-2018

Hypothesis paper: Mechanism for Primary Blast Induced Traumatic Brain Injury with Minimal Head Motion

Charles F. Babbs
Purdue University, babbs@purdue.edu

Hypothesis paper: Mechanism for Primary Blast Induced Traumatic Brain Injury with Minimal Head Motion

Charles F. Babbs, MD, PhD*

*Weldon School of Biomedical Engineering, Purdue University

October, 2018

Abstract

Transit of the human skull by blast waves produces diffuse brain injury. The exact mechanisms are unknown. This paper describes plausible mechanisms in which steep intracranial pressure gradients, demonstrated in prior computational models of blast-skull interaction, produce subsequent deformation and motion of the whole brain within the skull, without obvious movement of the head. Equations of motion are derived to describe the acceleration, velocity, and relative position of both the skull and the brain in response to known extracranial and intracranial pressures both during and several hundred milliseconds after blast wave passage. A finite element model is solved to visualize the resulting dynamics. Whole head displacement is minimal (~ 1 mm) during primary blast wave passage. However, the brain experiences intense acceleration during the first millisecond as the blast wave passes the head and is compressed and stretched for the next 10 to 20 msec, while moving through cerebrospinal fluid toward the inner aspect of the skull, at speeds near 0.5 m/sec. Then cycles of coup and contrecoup collision and rebound occur during the next several hundred milliseconds, producing maximal compressive strains of 20 percent or more. A quantitatively realistic causal sequence, demonstrated in a companion analytical model, includes passage of the shock wave in air past the rounded skull; compression of the skull; generation of intracranial sound waves and pressure gradients; distortion followed by acceleration of the whole brain through cerebrospinal fluid; collision of the brain with the inner aspect of the skull; compressive strain wave propagation through the brain with gross deformation, and subsequent diffuse axonal injury. This physics-based sequence, emphasizing whole brain motion through cerebrospinal fluid within the skull and playing out over much longer durations than are usually modeled, provides a unifying concept relating blast exposure levels to the risk of brain injury that may inform the design of future studies.

Key words: axonal injury, biomechanics, blast, bTBI, contrecoup, coup, IED, mathematical model, neurotrauma, primary blast injury, shock wave

Introduction

Blast induced neurotrauma (BINT) or blast-induced traumatic brain injury (bTBI) is a recognized disease entity, resulting most notably from explosions of improvised explosive devices (IEDs)[1-4]. Blast injuries can happen in four phases: (1) primary (direct effects of overpressure), (2) secondary (effects of projectiles/shrapnel), (3) tertiary (effects of falls from blast winds), and (4) quaternary (burns, and exposure to toxic gasses)[5]. Shielding by armored personnel carriers can protect soldiers from secondary, tertiary, and quaternary blast injury. However, shock waves can travel effectively through armor, such that sudden peak overpressures ~ 200 kPa still occur inside armored vehicles[6]. As a result, many soldiers have survived otherwise lethal blasts from IEDs only to suffer primary blast injury[7]. Blast-induced TBI is considered the signature injury for combat troops in today's military[8], accounting for nearly 70% of injuries in wounded service members in both Iraq and Afghanistan[1, 6].

The resulting pathology of "diffuse axonal injury" (DAI) has been observed in both laboratory and clinical studies of subjects suffering blast injuries[9]. For example, in Garman and coworkers' studies of anesthetized rats, the left side of the skull faced the 25% lethal blast waves[10]. Diffuse multi-focal axonal injury was observed, together with increased blood-brain-barrier permeability. Wang, Shi, and coworkers[11] in a mouse model found widespread multifocal neuronal and axonal degeneration in brains of blast exposed mice both in the cranio-caudal and coronal planes. Bauman and coworkers found widespread white matter fiber degeneration in swine models[2]. Evidence of diffuse axonal injury on integrated MRI and diffusion tensor imaging has been found as well in human patients suffering blast-related traumatic brain injury,[12-14] which is especially evident if the original injury is accompanied by loss of consciousness[15].

Defining the exact mechanisms that mediate primary bTBI, however, remains an open problem[2, 5, 6, 9, 16-18]. In particular, the widespread and diffuse injury induced by the blast wave, especially injury on the side of the brain opposite the source of the blast, is a phenomenon that has yet to be well understood[19]. Possible mechanisms that have been suggested include acoustic impedance mismatch, bubble formation, direct passage of the blast wave through the cranium, skull flexure from blast waves, shear strain, tensile strain, sudden translation of the head, micro-cavitation, blood surge from the torso following chest compression, air embolism from lung injury, intracranial bleeding, contrecoup contusion, blast wave transmission through the orbits and nasal sinuses, skull deformation with elastic rebound, "lens effects" due to the concave shape of the calvarium leading to complicated interference patterns of pressure waves, diffuse axonal injury, elongation of cell bodies, and micro-shear between cell nuclei other organelles[1, 2, 5, 20-27]. There is no consensus.

Previous papers from local colleagues describe and review experimental models and approaches to this problem[28-32]. The goal of the present study is to develop a simplified physics-based model for the underlying cause of primary blast injury that can be used to inform future research. A special focus, in contrast to previous studies which focused on the first 1 to 10 msec after blast exposure[17, 21, 23, 27, 33], is characterization of whole brain motion through the cerebrospinal fluid, collision of the brain with the rigid skull, and coup and contrecoup injury, occurring over time scales of several hundred msec after blast exposure. As the results will show, it is important to

consider this wider range of time scales to capture the full story of the biomechanics of blast induced traumatic brain injury.

Theory

Approach

The biomechanics of closed head injury in general, including impacts from falls, contact sports, and violence, as well as blast waves, are difficult to study experimentally. Harmful impacts last only 2 to 20 msec. Subsequent motion of the brain inside the skull lasts just a few seconds and is rarely seen. Such motion has been only partially revealed by studies in animals using high-speed photography through a lucite calvarium or high-speed fluoroscopy of implanted radiodense pellets[34-37]. Only occasionally are the brains of patients sustaining minor head injury examined at autopsy. Fortunately, mathematical analysis and modeling of the skull and brain in response to known pulses of head acceleration allow one to study a variety of conditions that are difficult, impossible, or unethical to reproduce in animals or in humans[6].

Blast overpressure vs. time curves[5, 11, 38] have an abrupt onset corresponding to passage of the hypersonic shock wave front past a fixed detector and a more gradual linear to exponential decline over a span of several milliseconds thereafter, as sketched in Fig. 1(a) for a typical case associated with neurotrauma. Using principles of classical Newtonian physics, the following analysis considers first the displacement of the whole head and skull during blast wave transit, without elaboration of its internal structures, and then interaction the shock wave with the internal structure of the brain, surrounded by the cerebrospinal fluid (CSF)-filled subarachnoid space and encased in the semi-rigid skull.

Linear motion of the whole skull

Consider the waveform for a blast-induced shock wave in air, as sketched in Fig. 1 (a). Overpressure is plotted as a function of time for a hypersonic shock wave passing a fixed point in space. The waveform is approximately triangular to decaying exponential[10] (Friedlander waveform), with small damped sinusoidal after-waves and amplitudes ranging from 0 to P_{max} (~500 kPa) on the vertical axis and from 0 to t_{max} (~ 1 to 5 msec) on the horizontal axis. Let v_s denote the velocity of the shock wave front in air (~ 500 m/sec)[39], which is significantly greater than normal sound speed in air (343 m/sec). In turn, the wavelength of the shock wave is $\lambda = v_s t_{max}$ (~ 0.5 to 2.5 meters) which is much greater than the diameter of the human head, and very much greater than the head dimensions of laboratory animals. (Note that this simple calculation casts doubt on proposed mechanisms involving reflection and summation of pressure waves within the skull.)

To estimate the motion of the whole head it will be sufficient to imagine a simple model of the head as a rectangular solid, having linear dimension, L in the direction of the blast and surface area, A (Fig. 1 (b)). This simplified model makes it easy to appreciate two phases of head motion. In the first phase the shock wave front is passing from the near side to the far side of the

model, as shown in Fig. 1 (c). Since $L < \lambda$ there is a right-to-left directed force on the head approximately equal to

$$F_1 \approx P_{max} A \,, \tag{1}$$

which lasts for a duration of $t_1 = L/v_s$ (~ 0.2 m / (500 m/sec) = 0.4 msec). Numerically $t_1 < t_{max}$. After the shock wave front passes the model, there will be a follow-on left-to-right directed force (Fig. 1 (d))

$$F_2 \approx P_{max} \frac{L}{\lambda} A = P_{max} \frac{v_s t_1}{v_s t_{max}} A = P_{max} \frac{t_1}{t_{max}} A \tag{2}$$

assuming here on average, a linear ramp for the downslope of the overpressure waveform, which is reasonable based on empirical measurements[5, 38]. (The linear ramp assumption can be eliminated, as shown in Appendix 1, at the cost of somewhat more algebra.) Thus, first, as the shock wave front passes around the head, the head will be pushed one way for a brief time, very strongly (phase 1, Fig. 1 (c)). Then, second, as the downslope of the shock wave passes the head, the head will be pushed the opposite way for a longer time, less strongly (phase 2, Fig. 1 (d)).

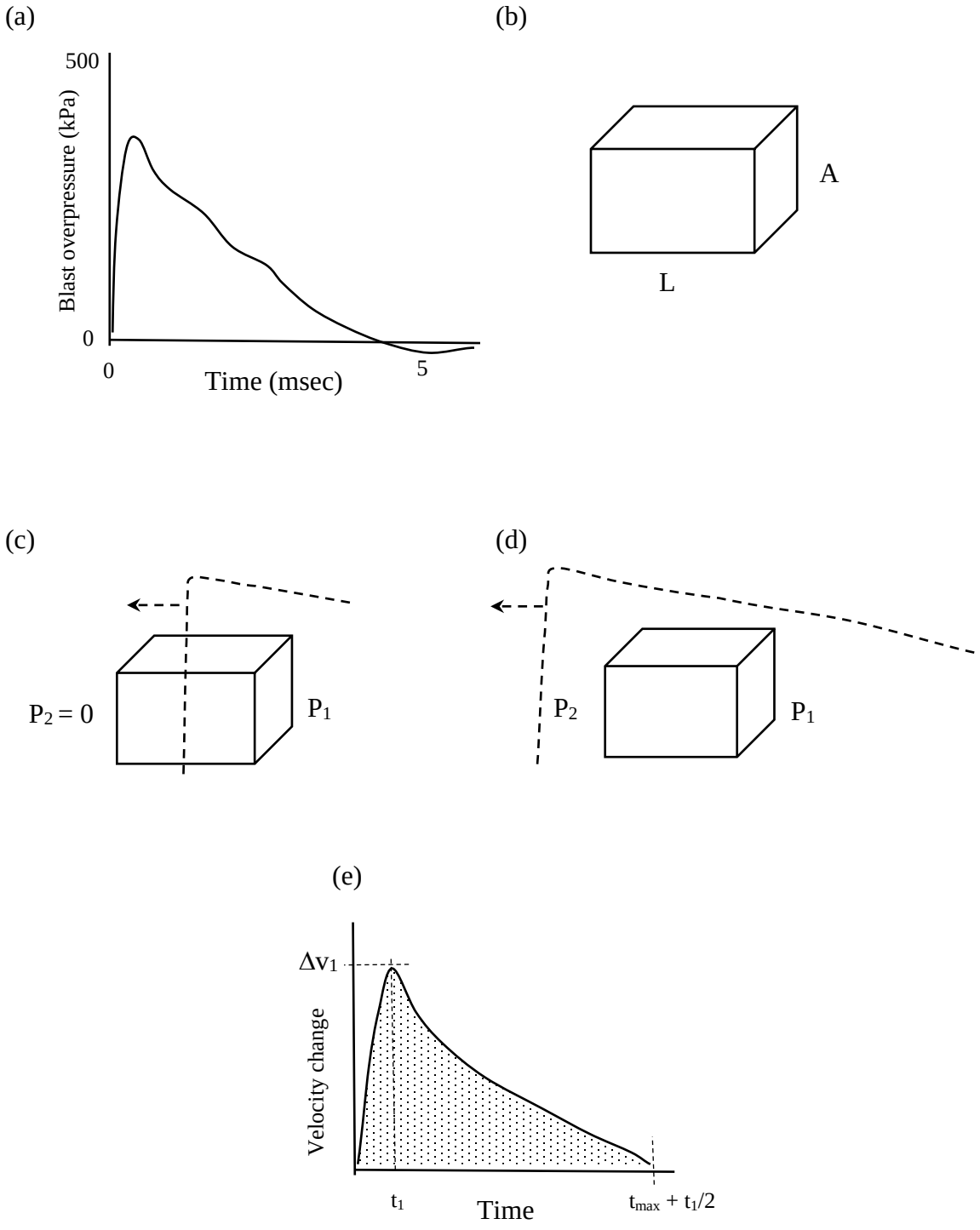

FIG 1. Sketches of blast wave interaction with "blockhead" model. (a) typical blast overpressure waveform, (b) blockhead model, (c) phase 1 – early passage of blast wave front (dashed line) with pressure $P_1 > P_2 = 0$, (d) phase 2 – later passage of blast wave downslope (dashed line) with pressure $P_1 < P_2$, (e) blockhead velocity vs. time; area under curve equals distance moved.

To estimate the net changes in velocity and net changes in position of the whole head one may apply Newton's second law, F = ma, or force equals mass times acceleration. The acceleration of the whole head having average mass density, ρ, during phase 1 is

$$a_1 = \frac{F_1}{m} = \frac{P_{max} A}{\rho A L} = \frac{P_{max}}{\rho L}. \quad (3)$$

The oppositely directed acceleration of the whole head having average mass density, ρ, during phase 2 is approximately

$$a_2 = \frac{F_2}{m} = -\frac{P_{max} \frac{t_1}{t_{max}} A}{\rho A L} = -\frac{P_{max}}{\rho L} \frac{t_1}{t_{max}} = -a_1 \frac{t_1}{t_{max}}. \quad (4)$$

The change in velocity of the head during phase 1 is

$$\Delta v_1 = a_1 t_1. \quad (5)$$

The oppositely directed change in velocity of the head during phase 2 is

$$\Delta v_2 \approx a_2 \left(t_{max} + \frac{1}{2} t_1 \right) = -a_1 \frac{t_1}{t_{max}} \left(t_{max} + \frac{1}{2} t_1 \right) \approx -a_1 t_1 = -\Delta v_1 \ . \quad (6)$$

Hence head velocity during complete transit of the shock wave has a form suggested in Fig. 1 (e). The head will be pushed forward a short distance, d, and then stop or nearly stop. One can estimate distance, d, as the area under the curve of Fig. 1 (e), namely

$$d = \frac{1}{2} \Delta v_1 \left(t_{max} + \frac{1}{2} t_1 \right) \approx \frac{1}{2} a_1 t_1 t_{max} = \frac{1}{2} \frac{P_{max}}{\rho L} t_1 t_{max} = \frac{1}{2} \frac{P_{max}}{\rho L} \frac{L}{v_s} t_{max} = \frac{1}{2} \frac{P_{max}}{\rho v_s} t_{max}. \quad (7)$$

Numerically, for example, using 200 kPa pressure and 1000 kg/m^3 as the density of the head (that of water) we have

$$d = \frac{1}{2} \frac{200{,}000 \frac{kg}{sec^2 m}}{1000 \frac{kg}{m^3} \cdot 500 \frac{m}{sec}} 0.005 \text{ sec} = 0.001 \text{ meters} \quad (8)$$

or 1 mm. This movement of about one millimeter in response to a powerful blast is a remarkably short translation, especially compared to the roughly 9 mm width of the fluid-filled subarachnoid space separating the surface of the human brain from the inner aspect of the skull. This nearly net zero effect is unlikely to be changed by any follow-on low amplitude, alternating positive and negative after-waves of primary overpressure in some blast waveforms. Note that Equations (7) and (8) describe effects of primary blast wave pressure only, not secondary or tertiary effects of projectiles or wind. Thus, movement of the skull alone is not sufficient to cause anatomic

deformation or damage to the brain in primary bTBI. Minimal skull motion during passage of pure shock waves has also been noted in more sophisticated multiscale dynamic models by Taylor and Ford[40] and has been observed experimentally at Purdue University for human head models, as seen in videos of laboratory studies (Tyler C. Robbins and Steven F. Son, unpublished observations).

Motion of the brain within the skull

To explain neurotrauma associated with pure primary blast injury, something beyond simple whole head translation is required. Clues come from laboratory measurements and computational models. For example, Sundaramurthy and coworkers (2012) using sophisticated intracranial pressure transducers, found waveforms like those in Fig. 1(a) lasting about 5 msec with peak initial pressures of 150 kPa (although the rat skull is extremely small and thin; more on this later). A clearer picture of spatial distributions of blast-induced intracranial pressure transients during shock wave passage comes from advanced computational models[17, 18, 21, 22, 25, 27, 40, 41]. A synthesis of results from such simulations, shown in Fig. 2, reveals a picture of time-averaged intracranial pressure distributions over the first 0.3 to 1 msec after contact of the hypersonic shock wave front with the human skull. During shock wave transit past the skull, pressure spikes on the order of 100 kPa to 500 kPa occur within the skull. Generally, computed intracranial pressures are greatest on the side of the blast and substantially lower on the far side[17, 21, 22, 25, 40, 41].

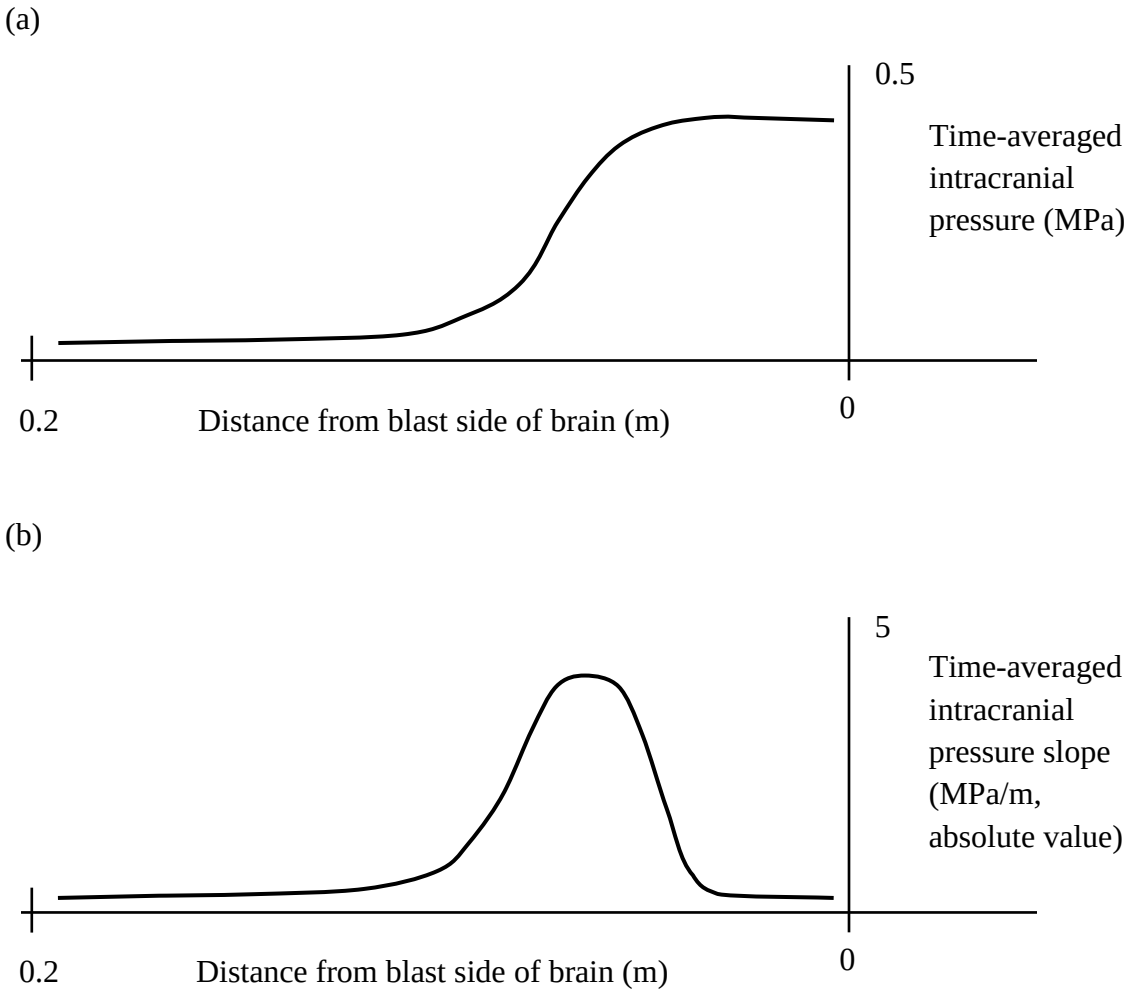

FIG. 2. Synthesis of multiple simulation studies of human intracranial pressure at sub-millisecond times after blast exposure. (a) absolute pressure, (b) pressure gradient. Blast on right side. Numerical values are approximate.

These intracranial pressure transients occur within semi-rigid, but not perfectly rigid, models of the skull, in which small circumferential compressive strains on the order of 0.05 percent have been measured[42]. Thus, local deformation of the semi-rigid skull permits transmission of sound pressure waves into the intracranial compartment. One may speculate, and also roughly calculate, that venting of pressure through the tentorium cerebelli into the posterior compartment and foramen magnum at the mid posterior base of the skull is in part responsible for the sharp drop off of near sided pressure peaks toward the middle of the brain. The resulting change in pressure as a function of distance creates steep spatial pressure gradients within the skull during the first millisecond or so after blast exposure.

The major insight motivating the present study is the hypothesis that these pressure gradients are strong enough to drive whole brain motion, leading to pathologically significant collisions with the inner aspect of the skull. The underlying biomechanics are easily studied, both in a simple box-shaped finite element model of blast-induced brain motion and deformation, which is described first, and in a companion analytical model, having a hemispherical geometry, which is described second.

Methods

Finite element model

Within the skull the brain is suspended in water density cerebrospinal fluid (CSF), which surrounds the human brain for a distance of about 9 mm on all sides prior to blast exposure. Here we assume that the Poisson's ratio for brain tissue is 0.5, so that neither brain volume nor CSF volume changes during moderate deformation. Fig. 3 illustrates a simple Voigt model of the brain composed of discrete springs, k, masses, m, and dampers, μ. The Voigt model of the brain is bracketed at each end by a 0.9 cm wide gap of cerebrospinal fluid, separating the brain model from hard-stop, boundaries, which are essentially rigid compared to brain tissue after shock wave passage. In this “1.5-dimensional” model, Poisson’s ratio expansion and contraction are accounted for in the dimensions perpendicular to the x-axis in Figure 3.

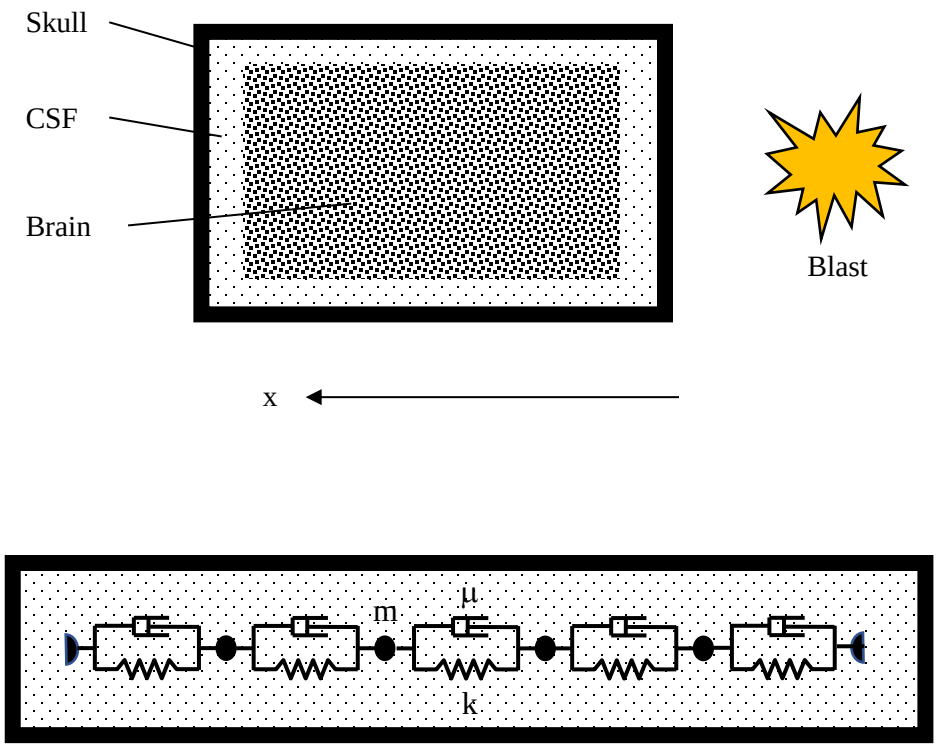

FIG. 3. Voigt model of the brain, cerebrospinal fluid filled subarachnoid space, and hard-stop boundaries of the cranium. Dimension x represents the direction of blast wave propagation (front-to-back unless otherwise specified). The viscoelastic brain is represented by discrete mass elements, m, springs, k, and dampers, μ. In the unstressed condition the masses, m, are separated by distance Δx_0. The cross section of the viscoelastic solid is A. Blast facing edge of model is at x = 0. For clarity, only a few finite elements are shown. End masses are one half interior masses. Motion occurs only in the x-dimension; however, Poisson's ratio expansion and contraction are accounted for in the dimensions perpendicular to the x-axis. Right and left skull edges are hard-stop boundaries. Viscosity of CSF is considered negligible, as previously demonstrated[43].

The objective here is to track the motion of each mass or node of the model in time during and after blast exposure. For an interior mass m, the x-component of acceleration depends upon the sum of applied forces, F_p, F_k, and F_μ , due respectively to local pressure gradients, neighboring springs, and neighboring dampers. Invoking Newton's second law of motion for interior node, n,

$$ma_n = F_p + F_k + F_\mu \, . \tag{9}$$

These expressions for each interior node, n, and the similar ones for the two end nodes of mass m/2, can be solved for the acceleration of each node in the array.

Driving forces on each finite element, n, having cross section A_n and thickness Δx_0, during early, sub-millisecond times with nonzero intracranial pressure gradients $\left(\frac{\partial P}{\partial x}\right)_n$ are given by

$$F_p = -A_n \left(\frac{\partial P}{\partial x}\right)_n \Delta x_0 = -V_n \left(\frac{\partial P}{\partial x}\right)_n \tag{10}$$

in terms of the local volume V_n and the local intracranial pressure gradient in the x-direction. In the absence of reactive forces from neighboring springs and dampers, the acceleration of node, n, subjected to local pressure gradient $\left(\frac{\partial P}{\partial x}\right)_n$ would be

$$a_n = \frac{F_p}{\rho V_n} = -\frac{1}{\rho}\left(\frac{\partial P}{\partial x}\right)_n . \tag{11}$$

As shown in detail in Appendix 2, the local node acceleration including reactive forces from the elastic elements or springs connecting a given interior node, n, with neighboring nodes n + 1 and n – 1, and from the corresponding dampers or viscous elements is

$$a_n = -\frac{1}{\rho}\left(\frac{\partial P}{\partial x}\right)_n + \frac{E}{\rho}\frac{\left(x_{n+1} + x_{n-1} - 2x_n\right)}{\left(\Delta x_0\right)^2} + \frac{D}{\rho}\frac{\left(v_{n+1} + v_{n-1} - 2v_n\right)}{\left(\Delta x_0\right)^2}, \tag{12}$$

where E is Young's modulus of elasticity (stiffness), D is the analogously defined damping modulus (D/E ≈ 0.01 sec), x_n is local node position, and v_n is local node velocity. In words, a_n = pressure gradient term + elastic recoil term + viscous damping term. For end nodes 1 and N the corresponding expressions are derived by most easily from Equation (12) using zero end force conditions. For end node 1 set $x_{n-1} = x_1 - \Delta x_0$, and for end node set N $x_{N+1} = x_N + \Delta x_0$. Similarly, for end node 1 set $v_{n-1} = v_1$, and for end node set N $v_{N+1} = v_N$. If computed points for end nodes move outside the boundary of the skull, they are brought back to the hard stop positions, and velocity is set to zero. To account for possible brain expansion in the orthogonal (y and z) dimensions according to Poisson's ratio, ν = 0.5, a maximal allowed compressive strain is enforced, $0.5\varepsilon_{max} = \frac{2 \times CSFwidth}{brain\ diameter}$, or $\varepsilon_{max} \approx 0.30$ with frictionless slippage in the x-dimension still allowed. This constraint describes physical limits on Poisson's ratio expansion imposed by the rigid boundaries of the skull.

Parameter values and boundary conditions

Brain tissue is considered to be a compressible, viscoelastic material. Viscoelastic properties of whole brain have been rather well studied over the past 30 years, and consensus values for Young's modulus of elasticity and for an analogously defined energy loss modulus can be gleaned from the literature[43-45]. Despite rather large variability in published values, these data provide a basis for a "baseline model" of typical brain viscoelastic properties that is sufficient for present purposes. They are summarized in Table 1. Since large strains are anticipated a simple nonlinear elasticity estimator was implemented as follows. Young's modulus (engineering stress divided by engineering strain) as a function of engineering strain, ε, and the small strain modulus, E_0 ,was computed as $E(\varepsilon) = \frac{E_0}{\cos^2(\varepsilon\pi/2)}$. For simplicity, the damping factor, D, is taken as a constant. Inclusion of damping can be used to explain the observed strain rate dependence of measured values of quasi-static E.[45] Relative motion of the brain is computed with respect to the boundaries of the skull in response to induced pressure gradients in Figure 2, using Equation (12). Thus, the dynamics of skull deformation are not described in this first numerical model, and the assumed rectangular shape of the model is satisfactory at this stage.

Table 1. Parameters of the baseline model

Variable name	**Definition**	**Numerical value**	**Units**
ρ_{brain}	Brain density	1046	kg/m^3
E_0	Young's elastic modulus of brain tissue (small strain value)	10,000	Pa
D	Damping modulus of brain tissue	100	Pa-sec
span	Total model span (brain + CSF)	0.18	m
A	Brain cross section	0.0144	m^2
h	CSF width	0.009	m
Δx_0	Finite element thickness	0.018	m
ν	Poisson's ratio	0.5	
p	Duration of intracranial pressure pulse	0.001	sec
maxdPdx	Maximal time-averaged intracranial pressure gradient in x-dimension	5×10^6	Pa/m
SDdPdx	Standard deviation of Gaussian curve of hypothetical intracranial pressure gradient in x-domain	0.02	m
Δt	Time step for numerical integration	0.00005	sec

In keeping with previous work (Table 2) a spatial average and time average hypothetical intracranial pressure gradient of 2.5 MPa/m lasting 1 msec and acting over 10 cm distance was chosen for the baseline model. The distribution of particular pressure gradient values in the x-dimension was approximately Gaussian, as shown in Fig. 2(b).

Table 2. Literature values for approximate intracranial pressure gradients.

Study	Pmaxair	Gradient	Distance	Pmax/2	Mean	Reference
	MPa#	duration	meters	MPa	Gradient	
		msec			MPa/m	
1	1.3	2	0.05	0.5	10	Taylor 2009[40]
2	0.1	2	0.15	0.1	0.6667	Moss 2009[25]
3	0.52	0.4	0.1	0.25	2.5	Moore 2009[21]
4	1.5	0.7	0.1	0.5	5	Nyelin 2010[41]
5	0.5	1--8	0.1	0.3	3	Panzer 2012[27]
6	0.7	1	0.1	0.3	3	Zhang 2013[33]
7	2	4	0.1	1.7	17	Jean 2014[17]
8	0.36	0.5	0.1	0.25	2.5	Taylor 2014[18]
Baseline Model	0.5	1	0.1	0.25	2.5	

Extracranial air pressure

Integration of the equations of motion

Beginning with initial conditions at t = 0, the horizontal accelerations are doubly integrated using the simple Euler method to extrapolate velocity, v_n , and position, x_n , of each node, n , from time t to time t + Δt, namely

$$v_n(t + \Delta t) = v_n(t) + a_n(t)\Delta t, \quad (13a)$$

$$x_n(t + \Delta t) = x_n(t) + v_n(t)\Delta t\,. \quad (13b)$$

Results are displayed in computer animations showing motion and expansion of all finite elements in the model as a function of time. The time step of integration, Δt, was small enough to permit faithful representation of strain wave propagation.

Computational methods

The forgoing numerical model was implemented in Visual Basic code within an Excel spreadsheet on ordinary personal computers operating under Microsoft Windows 10. Visual Basic provides a highly portable platform for custom animations to visualize brain motion. Computer code was validated by comparison with simple test cases and by testing for conservation of energy in the absence of damping.

To visualize motion of the model of the brain, the finite elements are represented on screen as tall rectangles that may undergo compression in the x-direction of the blast and corresponding Poisson's ratio expansion in the perpendicular y-dimension. The skull is represented as a rectangular box with an underlying space equal to the CSF width. A small number of thick finite elements ($\Delta x_0 = 0.6$ cm) permits visual appreciation of subtle local compression and elongation in the animated results.

At times $t > 0$ the brain model moves inside the skull in response to an impulse of acceleration caused by blast-induced pressure gradients, which are taken as inputs to initiate finite element dynamics. Drag forces on the brain moving these short distances through CSF are ignored[43]. Skull motion is assumed to be negligible. The skull boundaries are completely rigid. Motion of each brain slice or finite element with respect to the fixed boundaries of the skull is computed, and the maximum compressive strain experienced in any of the finite elements (typically an element directly impacting the skull) is saved as a descriptor of overall brain deformation under particular conditions.

Companion analytical model

To check the numerical results of the finite element model, a simple analytical model was derived to predict over all brain motion and deformation, and in particular the maximal compressive strain experienced by the leading edge of the brain after collision with the inner aspect of the skull. Somewhat surprisingly, this analytical approach can be used to describe a complete chain of causation extending from passage of the shock wave in air past the skull, to compression of curved cranial bone, to generation of intracranial sound waves in aqueous cerebrospinal fluid and brain, to creation of brief, intense pressure gradients within the skull, to acceleration of the whole brain through cerebrospinal fluid by the pressure gradients, to collision of the brain with the inner aspect of the skull, consequent strain wave propagation through brain substance, and accompanying deformation that is likely to cause diffuse axonal injury. For simple geometric cases, in particular a hemispherical skull, each of these steps in the chain can be described straightforwardly by an equation based on classical Newtonian physics.

Bone compression by airborne shock wave passage

Combining the Law of Laplace for a thin walled spherical, or hemispherical, pressure vessel as a model of the calvarium with the definition of Young's modulus of elasticity E = stress/strain for

bone, one obtains the circumferential or radial strain, $\bar{\varepsilon}_{skull}$, in a skull of radius, r, and thickness, h, in response to a brief, blast-induced pressure difference, $\overline{\Delta P}_{skull}$, namely

$$\bar{\varepsilon}_{skull} = \frac{1}{2}\frac{\overline{\Delta P}_{skull}}{E_{skull}}\frac{r}{h}, \tag{14a}$$

where $\bar{\varepsilon}_{skull}$ and $\overline{\Delta P}_{skull}$ are the time averaged values over the duration of the blast wave passage. Owing to the high stiffness, E, of bone (8×10^9 Pa)[46], the quasi-static assumption implicit in Equation (14a) is reasonable. That is, skull flexure, or shock wave propagation through the skull is instantaneous in this treatment--much faster than either shock wave propagation in air or the resulting strain wave propagation in the brain. (This feature, as will be shown, allows a mechanism for brain distortion during primary blast injury without the need to account for strain propagation through the cranium before the arrival shock or stress waves through brain tissue.)

As a typical numerical example, the radial or circumferential blast-induced compressive strain in the skull would be

$$\bar{\varepsilon}_{skull} = \frac{1}{2}\frac{200000\ \text{Pa}}{8 \times 10^9\ \text{Pa}}25 = 0.00031 \tag{14b}$$

or 0.03 percent compressive strain. This value is comparable with the laboratory observations of 0.01 to 0.06 percent compression of the skull during blast wave passage[42]. In turn, the time-averaged amplitude of radial skull compression in units of length (meters) is $\bar{s} = \bar{\varepsilon}_{skull}\, r$.

Intracranial sound waves

Displacement of the skull by distance, $\bar{s}$, creates a compression wave, or sound wave, in the underlying cerebrospinal fluid and brain. For a classical sound wave propagating in water or in brain of mass density ρ in which the sound speed is that in water, v_w, the time-averaged pressure generated in water is

$$\overline{\Delta P}_w = v_w \rho \omega \bar{s}, \tag{15}$$

where the angular frequency $\omega = 2\pi/T$ for wave period T. Combining the above,

$$\overline{\Delta P}_w = \frac{2\pi}{T} v_w \rho \bar{\varepsilon}_{skull} r\ . \tag{16a}$$

As a numerical example, the expected intracranial pressure rise for a T = 3 msec duration blast wave, using the mass density and sound speed for water, would be

$$\overline{\Delta P}_w = \frac{6.28}{0.003\ \text{sec}}1500\ \frac{m}{sec}1000\ \frac{kg}{m^3}0.0003\ \cdot\ 0.1\ \text{m}\ =\ 94\ \text{kPa}\ . \tag{16b}$$

This value is in keeping with experimentally recorded intracranial pressures of about 100 kPa[11].

Expanding Equation (16a) in terms of fundamental model variables, using Equation (14a),

$$\overline{\Delta P}_w = \frac{\pi}{T} v_w \rho \frac{\overline{\Delta P}_{skull}}{E_{skull}} \frac{r}{h} r \,. \tag{17}$$

Intracranial pressure gradients

Realizing that pressure within the skull tends to be maximal at the periphery on the blast side, falling to near zero near the center of the brain[17, 21, 22, 27, 40] (perhaps due to pressure venting into the posterior fossa and spinal canal) one can rearrange Equation (17) to estimate the time-averaged pressure gradient in the near-side half of the intracranial space as

$$\overline{\left(\frac{\partial P}{\partial x}\right)} \approx \frac{\overline{\Delta P}_w}{r} = \frac{\pi}{T} v_w \rho \frac{\overline{\Delta P}_{skull}}{E_{skull}} \frac{r}{h} \,. \tag{18a}$$

Given the roughly triangular wave shape of transcranial pressure during blast wave passage (Fig. 1(a)) one can estimate the time-averaged mean compression pressure, $\overline{\Delta P}_{skull} \approx \frac{1}{2} \Delta P_{max}$. Then

$$\overline{\left(\frac{\partial P}{\partial x}\right)} \approx \frac{\pi}{2T} v_w \rho \frac{\overline{\Delta P}_{max}}{E_{skull}} \frac{r}{h} \,. \tag{18b}$$

Whole brain acceleration

In turn, as shown in Equation (11), the magnitude of the acceleration of the near side half of the brain, which is subjected to the pressure gradient, $\overline{\left(\frac{\partial P}{\partial x}\right)}$, if isolated from the far side half, would be $\frac{1}{\rho}\overline{\left(\frac{\partial P}{\partial x}\right)}$, and the time-averaged acceleration of the whole brain, having twice the mass and subjected to the same forces, directed away from the side of the blast, would be

$$\bar{a}_{brain} = \frac{1}{2\rho}\overline{\left(\frac{\partial P}{\partial x}\right)} \approx \frac{\pi}{4T} v_w \frac{\Delta P_{max}}{E_{skull}} \frac{r}{h} \,. \tag{19}$$

The approximate change in velocity of the whole brain accelerated in this way for a single shock wave period, T, is $\bar{a}_{brain} T$ or

$$\Delta v_{brain} \approx \frac{\pi}{4} v_w \frac{\Delta P_{max}}{E_{skull}} \frac{r}{h} \,. \tag{20}$$

Collision, stain wave propagation, and motion after brain-skull contact

After brain-skull contact there is propagation of a compressive strain wave through the whole brain, accompanied by lateral expansion in dimensions orthogonal to the compression, according to Poisson's ratio. The strain wave is a wave of deformation within a soft elastic material that propagates much slower than do sound waves in water. In their 1994 textbook, ***The Mechanisms of Continua and Wave Dynamics***, Brekhovskikh and Gancharov[47] have described

the exact nature of the compressive strain wave in a column of elastic material impacting a rigid wall at constant velocity. They show that for a column of density, ρ, having uniform stiffness (Young's modulus of elasticity) E, and hitting a rigid wall with initial velocity, v_0, a wave of compressive strain is propagated through the column in a particular last-in/first-out pattern.

Fig. 4 illustrates Brekhovskikh—Gancharov compression of a uniform elastic column. An elastic column of length, L, hits a rigid wall with initial velocity v_0. The wall acts on the column with a force that initiates a strain wave, which propagates back along the column with wave speed $c = \sqrt{E/\rho}$. For this idealized one-dimensional case with no viscous damping or energy loss, the compression is of uniform degree in the compressed region and is zero elsewhere. A rectangular wave of compression and lateral expansion travels from the wall toward the free end of the column. The time required for the compression wave to reach the far end of the elastic column is $L/(c + v_0)$. (For blast exposed head models $c/ v_0 \sim 3$.) At this point the entire column is uniformly compressed. Thereafter, there is recoil, in reverse order, beginning with the free end. After another strain wave propagation time of $L/(c + v_0)$ the entire column moves in the opposite direction with velocity $-v_0$.

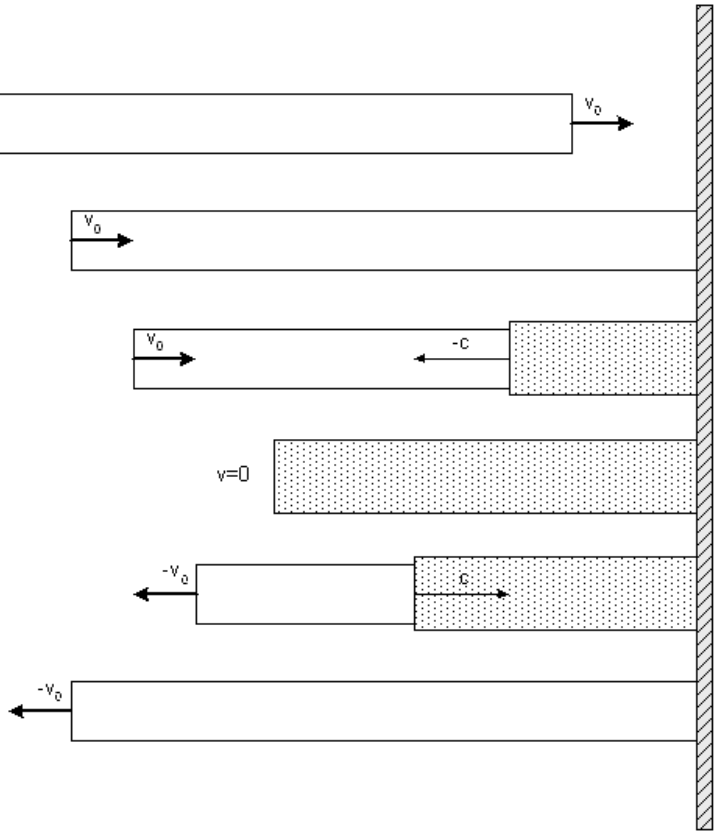

FIG. 4. Phases of motion of an elastic bar hitting a solid wall with initial velocity, v_0. Propagation of a compressive strain wave (shading) is shown at successive times after impact from top to bottom.

Maximal compressive strain

Realizing the last-in/first-out pattern of strain wave propagation of a rectangular elastic body hitting a solid wall with incoming velocity, $v_0 = \Delta v_{brain}$, one can use simple conservation of energy to derive an expression for maximal strain ε_{max} for the case of zero damping. Equating incoming kinetic energy with potential energy at maximal compression, ΔL, of a rectangular elastic solid with Young's modulus E, length L, and cross section, A, and spring constant, k = EA/L (see reference[48], also Appendix 2, Equation (31)), we have

$$\frac{1}{2}m(\Delta v_{brain})^2 = \frac{1}{2}k(\Delta L)^2 = \frac{1}{2}\frac{E_{brain}A}{L}(L\varepsilon_{max})^2 . \quad (21)$$

Substituting for the mass in terms of mass density, ρ,

$$\frac{1}{2}\rho AL(\Delta v_{brain})^2 = \frac{1}{2}\frac{E_{brain}A}{L}(L\varepsilon_{max})^2, \quad (22)$$

which leads to

$$\varepsilon_{max} = \Delta v_{brain}\sqrt{\frac{\rho}{E_{brain}}} . \quad (23)$$

Now, ignoring damping for the early part of the first impact, ignoring any small drag forces on the brain as it traverses the subarachnoid space[43], as before, and substituting for Δv_{brain} using Equation (20), we have

$$\varepsilon_{max} \approx \frac{\pi}{4} v_w \frac{\Delta P_{max}}{E_{skull}} \frac{r}{h} \sqrt{\frac{\rho}{E_{brain}}} . \quad (24)$$

Equations (14) through (24) describe quantitatively (for simple geometric cases) the complete chain of causation from passage of a blast wave in air past the head to potentially damaging gross deformation of the brain. These independently derived analytical expressions may be used to check results of the finite element model.

Note especially in Equation (24) that the maximal compressive strain, ε_{max} , is scale independent for similarly shaped skulls (r/h = constant), comprised of similar bone material (E_{skull} = constant) and exposed to similar blast overpressures in air (ΔP_{max} = constant). Expression (24) thus incorporates a scaling law relating blast wave intensity to the expected mechanical response of brain tissue across species. This result suggests that roughly similar pathology of blast induced neurotrauma can be expected in experimental models ranging in size from mouse to man.

Results

Baseline finite element model

Figures 5 and 6 show a series of snapshots in time depicting brain motion and deformation following blast exposure in the baseline model of Tables 1 and 2. In Figs. 5 and 6 the outer box represents the inner aspect of the skull. The underlying gap represents the CSF filled subarachnoid space. The colored inner rectangles represent slices of brain tissue modeled as Voigt bodies of defined thickness and cross section, having specified elastic and damping moduli (Table 1). Each rectangle represents the space occupied by particular viscoelastic elements between the center points of two nodes in Fig. 3. The crosshatched boundary (right) indicates the direction of the blast. The blast wave in air travels from right to left. During the first millisecond of simulation pressure gradients appear within the brain as shown in Fig. 2, which accelerate individual finite elements according to the pressure differences across them. The resulting motions of the finite elements of the brain model with respect to the fixed and rigid skull are depicted in Fig. 5 for early times and in Fig. 6 for later times.

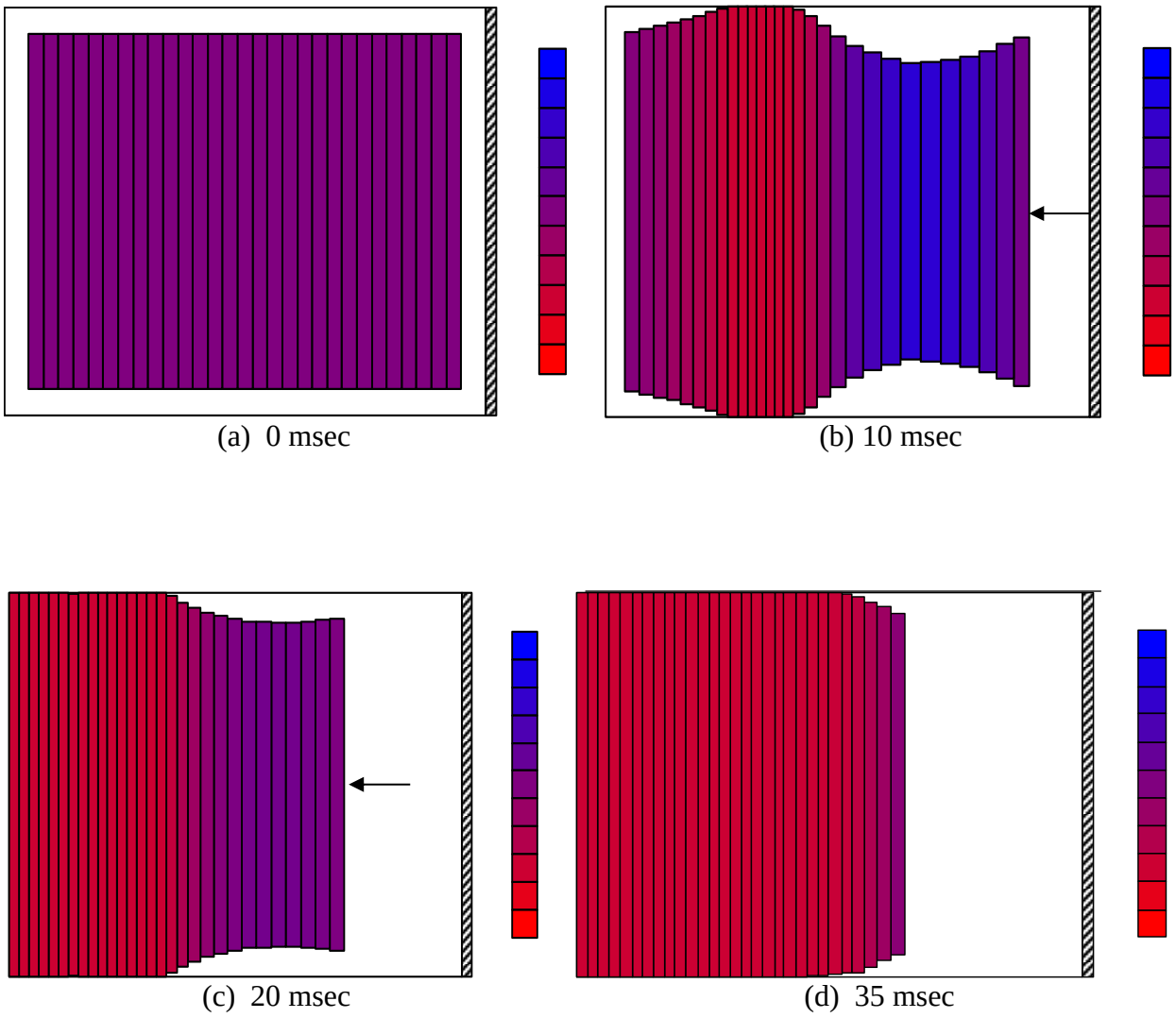

FIG. 5. Time series snapshots of deformation of a simple numerical brain model during early times after blast wave transit. Blast wave travels from right to left. Color bar represents strains ranging from –0.5 (red, compressive strain) to +0.5 (blue, elongation strain) in increments of 0.1. (a) resting state; (b) 10 msec after onset of intracranial pressure pulse, (c) 20 msec after onset of intracranial pressure pulse, (d) near maximum compression and zero velocity. Arrows indicate direction of whole brain motion. For further explanation see text.

Fig. 5 shows forward progress of the brain in the direction of blast wave propagation. Times of specific frames are indicated in msec from the onset of the intracranial pressure wave. At zero msec (a) the brain is at rest in a centered position. From 0 to 1 msec the brain is strongly accelerated by local pressure gradients, centered between the midpoint and the right edge of the model. At 10 msec (b) an internal strain wave is evident, moving from right to left, after the mid-right sections of the model are pushed into the static left half, followed by internal strain wave propagation. There are regions of compressive strain (middle, left) and elongation strain (middle, right). These strains are quite similar to those calculated by Chafi and coworkers[23] at such early times using a much more complicated three-dimensional finite element model. The early intraparenchymal strain wave continues to move to the left at 10 msec (b), while at the same time the whole brain begins to transit the subarachnoid space from right to left at a constant velocity of ~0.5 m/sec.

Importantly, the complete time history of brain deformation continues for much longer. Collision with the inner aspect of the skull opposite the side of the blast happens at about 16 msec, followed by reverse strain wave propagation, shown at 20 msec in Fig. 5(c). At 35 msec after blast onset (Fig. 5 (d)) the brain becomes maximally compressed against the skull. In this example the maximal compressive strain is 30 percent, the maximum allowed by the rigid boundaries of the skull (black rectangle). Corresponding lateral expansion in the second and third dimensions perpendicular to the compressive strain, as specified by Poisson's ratio of 0.5, is indicated by vertical elongation of the individual finite elements. This severe distortion provides an anatomic substrate for diffuse axonal injury, as observed in vivo by Inglase and coworkers[49] and by Garman and coworkers[10], among others.

Next the brain begins to recoil in the opposite direction owing to its elastic properties, as shown in Fig. 6 (a) at 50 msec. Then the brain re-crosses the subarachnoid space (Fig. 6((b)). Reverse transit speed is slower, owing to energy absorption by damping. Next the brain compresses against the inner aspect of the skull on the side of the blast (c). The second compression involving the right-hand half of the brain model is substantial, but quantitively less than compression on the first hit, here in the range of 20 percent compressive strain. This rebound collision may produce a contrecoup type injury. Taken together, the original coup injury and contrecoup injury (in the case of blast, the coup happening first on the side opposite the blast) create substantial anatomic distortion of the entire brain on both far and near sides. This is exactly the type of strain pattern that would be expected to produce widespread diffuse axonal injury. After the second impact there is further attenuated follow-on recoil (d), and depending on the degree of damping, there may be additional rounds of collision and recoil with progressively diminishing intensity. Thus, potentially injurious deformation and motion of the brain continue for hundreds of milliseconds after the blast wave has passed by the head, all driven by the initial steep pressure gradients on the near side of the intracranial compartment, lasting in this case just 1 msec.

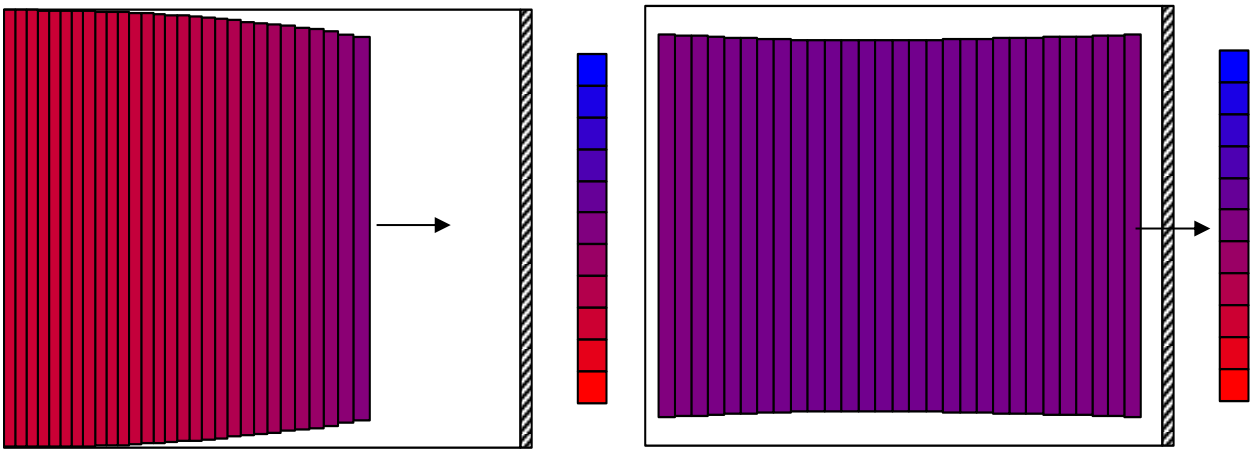

(a) 50 msec (b) 100 msec

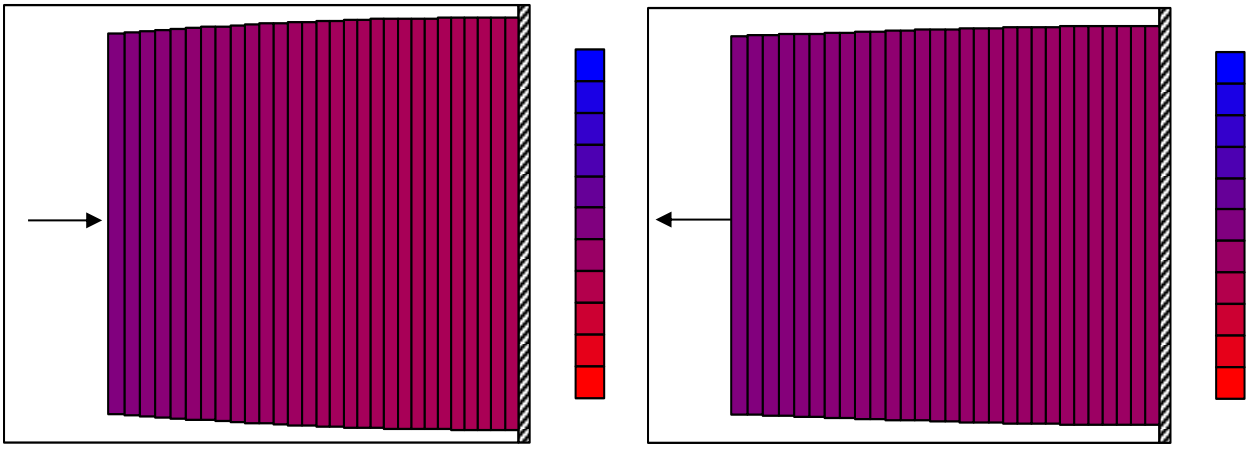

(c) 150 msec (d) 200 msec

FIG. 6. Time series snapshots of deformation of a numerical brain model after blast wave transit. Blast wave travels from right to left. The red to red blue change represents the range of local engineering strain (–0.5 for red, +0.5 for blue). (a) initial recoil with reverse motion, (b) reverse transit toward blast side, (c) early compression on blast side, (d) second recoil with original forward motion. Arrows indicate direction of whole brain motion. For further explanation see text.

Baseline analytical model

Similar results are obtained for the companion analytical model, which has the advantage of linking external blast wave pressure in air with internal brain motion according to a detailed causal sequence.

Brain motion, deformation, and compressive strain

Using Equation (20), namely $\Delta v_{brain} \approx \frac{\pi}{4} v_w \frac{\Delta P_{max}}{E_{skull}} \frac{r}{h}$, sec with sound speed in aqueous cerebrospinal fluid and brain at 40 ^oC, v_w = 1525 m/sec, a skull radius to thickness ratio, r/h = 25, maximum blast wave sound pressure, ΔP_{max} = 250 kPa (half maximal peak survival pressures[3, 10, 39]), and Young's modulus of skull, E_{skull} = 8 x10^9 Pa, one obtains an initial brain velocity toward the opposite side of the skull of 0.94 m/sec. Fig. 7 illustrates solutions for whole brain acceleration, collision, and strain wave propagation in the analytical model, based on an idealized collision of an elastic column with a rigid wall[43, 47], as shown in Fig. 4. The blast wave comes from the right side of the model, at the thicker, crosshatched boundary. The physics of Equations (14) through (18) are used to predict intracranial pressure gradients as a function of blast wave overpressure in air outside the curved skull. As before, time zero (Fig 7 (a)) indicates the beginning of intracranial pressure gradients, which last 1.0 msec. In this model, for simplicity, early-time internal strain waves through brain tissue before the first wall impact are not described.

After acceleration by intracranial pressure gradients, the whole brain completely traverses the subarachnoid space (Fig. 7(b)) and collides with the inner aspect of the skull at a time of about 11 msec. With strain wave velocity of $c = \sqrt{E/\rho}$ = 3.1 mm/msec and whole brain velocity v_0 = 0.94 mm/msec, it takes 162/(3.1 + 0.94) = 40 additional msec for the strain wave to back-propagate through the entire brain, as shown part way in this journey at 30 msec in (c). Lateral expansion is indicated by vertical elongation, associated with horizontal compression in the x-dimension. The maximal compressive strain is 30 percent. After the strain wave has propagated through the entire brain, recoil begins. At 75 msec reverse strain wave propagation is in progress (d), after which liftoff occurs, followed by reverse transit of the subarachnoid space (e). The brain then proceeds to impact the opposite wall, where another cycle of compression (f) and subsequent recoil occurs.

Interestingly, the position of the analytical model at 100 msec shown in Figure 7 (e) is nearly identical to the position of the finite element model at 100 msec shown in Figure 6 (b), despite the difference in initial, whole brain velocities at 1 msec, namely 0.5 m/sec for the finite element model vs. 0.94 m/sec for the analytical model. In the finite element model there is substantial internal strain energy at the 5 and 10 msec time points, as shown in Figure 5 (b) and (c). In turn, there is less kinetic energy of forward motion. The analytical model does not include internal deformation, so that all energy is kinetic energy prior to impact. Hence there is greater forward speed. However, at the point of maximal compression after the first wall hit, both models have zero whole brain velocity and zero kinetic energy. Thereafter, recoil is similar, as shown at 100 msec, except for a small energy loss due to damping in the finite element model. In general, the events in Fig. 7 are qualitatively and quantitatively similar to those for the finite element model

in Figs. 5 and 6, the major differences being that the analytical model does not include any damping or early-time internal strains. In this way the mechanics of brain motion and deformation after blast exposure are predicted by a second analytical line of reasoning, which is largely independent of the assumptions inherent in the finite element model.

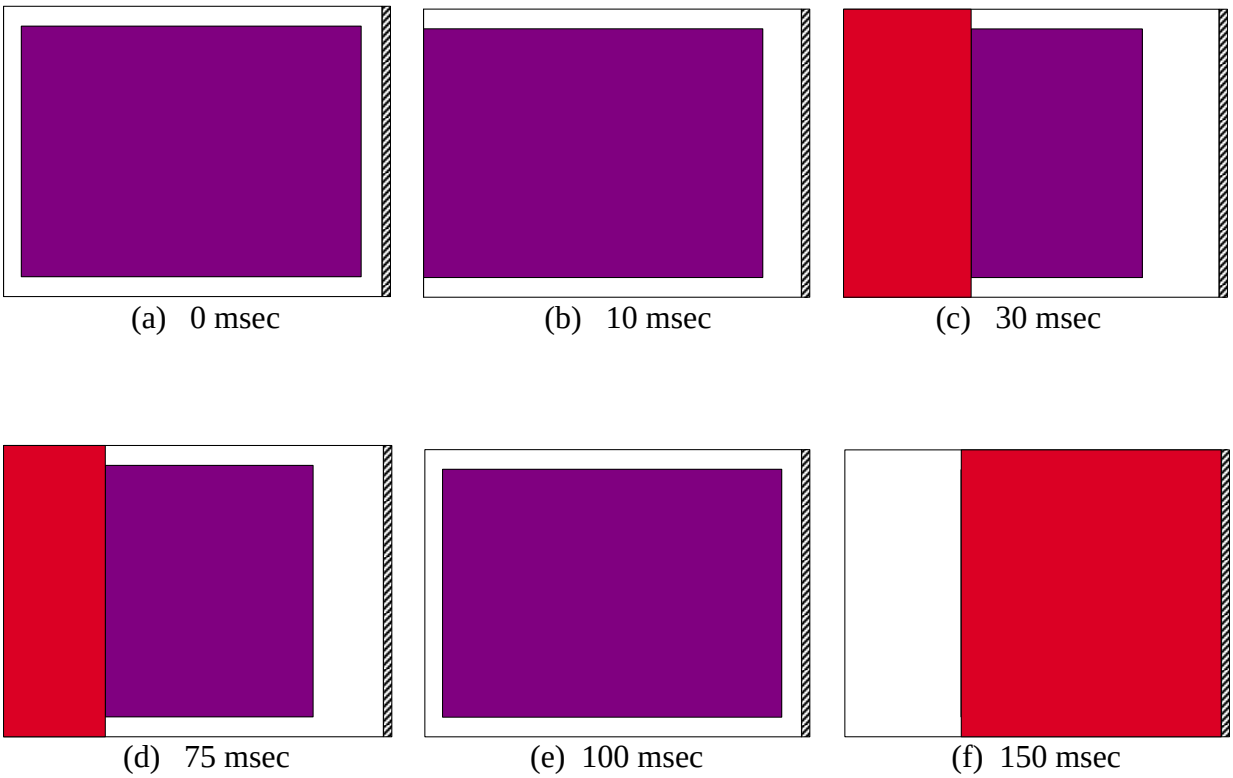

FIG. 7. Time series snapshots of deformation of the analytical brain model during and after blast wave transit. Blast wave travels from right to left. In (a), (b), and (c) whole brain motion is from right to left. In (d), (e), and (f) whole brain motion is from left to right. The purple to red color change represents the range of local compressive strain in the horizontal dimension (0% for purple, 30% for red). (a) start of impulse, (b) near first wall contact, (c) first collision with stain wave propagation, (d) first recoil, (e) reverse transit (f) second collision, maximum compression.

Discussion

The present biomechanical analysis and numerical simulations demonstrate that there can be gross motion and deformation of the brain within the skull, even though, paradoxically, there is little or no motion of the head. Further, primary blast injury may occur, not only during the first few milliseconds, as the blast wave propagates around the head, but also during the subsequent hundreds of milliseconds, as the whole brain collides with the inside of the cranium. In this proposed mechanism the brief, strong acceleration of the near side of the brain, produced by blast induced intracranial pressure gradients, drives the brain across the roughly 1 cm wide gap of the CSF-filled subarachnoid space at speeds approaching 1 meter/sec, after which it impacts the relatively rigid skull. Upon impact a compressive strain wave propagates through the whole brain, with maximum compression of about 30 percent, followed by rebound and one or more cycles of "coup" and "contrecoup" collisions.

The present numerical results illustrate this mechanism, beginning with well-established intracranial pressure distributions from prior studies and Newton's laws of motion in a Voigt model of the brain and skull. The results illustrate how there can be widespread damage throughout the brain, even though measured and computed intracranial pressures are highly asymmetrical and located predominantly on the near side of the blast. Damaging deformation of the brain can occur not only during early times (0 to 20 msec) owing to inhomogeneous local pressure gradients, but also during later times (20 to 200 msec) owing to coup and contrecoup collisions.

The companion analytical results show how such intracranial pressure distributions may result from simple elastic compression of the curved outer skull, vented through the posterior fossa and foramen magnum, and how the brain moves and recoils predictably as an elastic body suspended in cerebrospinal fluid between the near and far rigid walls of the skull, the whole process resulting in cycles of substantial compressive strain. The analytical expressions derived from fundamental physics also outline a complete chain of causation from blast wave propagation in air to profound deformation of brain tissue, which is very likely produce diffuse axonal injury. In addition, they provide a scale-independent equation for maximal compressive strain in animals with similarly shaped skulls (r/h = constant) and similar skull bone stiffnesses (E = constant). Moreover, the analytical result embodied in Equation (24), namely

$$\varepsilon_{max} \approx \frac{\pi}{4} V_w \frac{\Delta P_{max}}{E_{skull}} \frac{r}{h} \sqrt{\frac{\rho}{E_{brain}}} \qquad (24)$$

implies a full sensitivity analysis in a nutshell, describing quantitatively the relative influence of particular model parameters on the maximal compressive strain, ε_{max} , experienced by brain tissue.

The intent of the present paper is merely to propose a hypothesis. The work is clearly limited by the simplifying assumptions of the analysis. Follow on research might include full three-dimensional finite element simulations with detailed brain anatomy and varying constitutive properties at later times than those studied heretofore, further study of the physics and mechanics

that create intracranial pressure during blast exposure, including details of skull deformation caused by blast accompanied by venting of pressure through the posterior fossa and foramen magnum, effects of local differences in skull thickness and microanatomy and of shock waves travelling in different directions, and on a larger scale, more complex shock wave patterns obtained in closed rooms and spaces involving interferences of multiply reflected shock waves. Nevertheless, the present analysis and numerical simulations capture the essence of a physics-based mechanism producing primary blast induced neurotrauma that has not, to the author's knowledge, been described previously for durations beyond 10 msec. The proposed mechanism suggests which ways the whole brain moves, how long the whole brain moves, how much the brain is distorted, and which wave physics variables most directly determine brain injury. This mechanism of strain wave propagation through the whole brain and coup-contrecoup type motion explains heretofore puzzling occurrence of distant injury induced by blast waves, especially injury at the opposite side of the brain from wave entry[19, 50, 51]. Further analysis, such as that suggested by the present author for acceleration injury[43], may even allow one to identify threshold conditions for mild traumatic brain injury in a way that informs best practices for its prevention.

Appendix 1: general treatment of head acceleration by a blast wave

Let L be the length of the "blockhead" rectangular solid model in the direction of the blast, A be the cross section, m be the mass of the head, v_s be the shock wave velocity, t be time, 0 be the time when the shock wave front reaches the near side of the head, $t_1 = L/v_s$ be the time when the shock wave reaches the far side of the head, and t_{max} be the time when the positive overpressure phase of the shock wave passes the entire head. The rising phase of the blast overpressure vs. time curve is steep and nearly instantaneous, reaching a maximum value of P_{max}. The falling phase of the blast overpressure vs. time curve is of arbitrary shape and much longer, with $t_{max} >> t_1$. For times $t < t_1$ the positive pressure difference on the "blockhead" rectangular solid model, driving it forward, away from the blast, is approximately P_{max} , and the positive force is approximately AP_{max} . For times $t > t_1$ the negative or reverse pressure difference on the "blockhead" rectangular solid model, is

$$\Delta P(t) = P(t + L/v_s) - P(t) = P(t + t_1) - P(t) \approx \frac{dP\left(t+\frac{1}{2}t_1\right)}{dt} t_1 \ . \tag{25}$$

The reverse force on the model is $F_2 = \Delta P(t)A$, or

$$F_2 \approx A \frac{dP\left(t+\frac{1}{2}t_1\right)}{dt} t_1 \ . \tag{26}$$

By Newton's second law $F_2(t)dt = mdv$ for incremental velocity, dv, and time, dt. The total change in velocity in the reverse direction

$$\Delta v_2 = \int_{t_1}^{t_{max}+\frac{1}{2}t_1} dv \approx \int_{t_1}^{t_{max}+\frac{1}{2}t_1} \frac{F_2}{m} dt = \frac{A}{m} t_1 \int_{t_1}^{t_{max}+\frac{1}{2}t_1} \frac{dP\left(t+\frac{1}{2}t_1\right)}{dt} dt \ < 0. \tag{27}$$

Now for $t_1/2 << t_{max}$, as in a typical blast waveform passing the head, the integral in Equation (27) is approximately P_{max}, so that

$$\Delta v_2 \approx \frac{A}{m} t_1 P_{max} \approx -\Delta v_1 \,, \tag{28}$$

where Δv_1 is forward change in velocity that occurs as the blast wave front transits the head with near maximal overpressure on one side and zero overpressure on the other.

Appendix 2: including reactive elastic and viscous forces in the Voigt model

To include the reactive forces from the elastic elements or springs connecting a given node, n, with neighboring nodes n + 1 and n – 1, we have the balance of forces in the x-dimension on node n

$$\begin{aligned} F_{net} &= -V_n\left(\frac{\partial P}{\partial x}\right)_n - k\left(\Delta x_0 - \left(x_{n+1} - x_n\right)\right) + k\left(\Delta x_0 - \left(x_n - x_{n-1}\right)\right) \\ &= -V_n\left(\frac{\partial P}{\partial x}\right)_n + k\left(x_{n+1} + x_{n-1} - 2x_n\right) \end{aligned} \tag{29}$$

By Newton's second law the acceleration, $a_n = F_{net}/m$ or

$$a_n = -\frac{V_n}{m}\left(\frac{\partial P}{\partial x}\right)_n + \frac{k}{m}\left(x_{n+1} + x_{n-1} - 2x_n\right) . \tag{30}$$

From the definition of mass density, $m = \rho A_n \Delta x_0 = \rho V$. From the definition of Young's modulus,

$$E = \text{stress/strain} = \frac{\frac{k\Delta x}{A}}{\frac{\Delta x}{\Delta x_0}} = \frac{k\Delta x_0}{A} . \tag{31}$$

In turn,

$$k = \frac{EA_n}{\Delta x_0} , \tag{32a}$$

so that

$$\frac{k}{m} = \frac{E}{\rho(\Delta x_0)^2}. \tag{32b}$$

In terms of material density and Young's modulus,

$$a_n = -\frac{1}{\rho}\left(\frac{\partial P}{\partial x}\right)_n + \frac{E}{\rho}\frac{\left(x_{n+1} + x_{n-1} - 2x_n\right)}{\left(\Delta x_0\right)^2}. \tag{33}$$

To upgrade to a viscoelastic Voigt model, let u be the separation of two finite elements. If this local section is stretched a distance Δu at a rate $d(\Delta u)/dt$ the viscoelastic material creates a restoring force that opposes compression of the form

$$F = k\Delta u + \mu\frac{d\Delta u}{dt}. \tag{34}$$

This restoring force depends on the rate of elongation or compression according to the damping constant, μ. (Note the above equation holds if both Δu and $d(\Delta u)/dt$ are negative in compression.)

The viscous force on node n

$$F_\mu = \mu\left(v_{n+1} - v_n\right) + \mu\left(v_n - v_{n-1}\right) = \mu\left(v_{n+1} + v_{n-1} - 2v_n\right), \tag{35}$$

where $\mu = \frac{DA}{\Delta x_0}$.

By Newton's second law

$$a_n = -\frac{1}{\rho}\left(\frac{\partial P}{\partial x}\right)_n + \frac{k}{m}\left(x_{n+1} + x_{n-1} - 2x_n\right) + \frac{\mu}{m}\left(v_{n+1} + v_{n-1} - 2v_n\right). \tag{36}$$

From the definition of mass density,

$$\frac{k}{m} = \frac{E}{\rho(\Delta x_0)^2} \quad \text{and} \quad \frac{\mu}{m} = \frac{D}{\rho(\Delta x_0)^2}. \tag{37}$$

So, in terms of material properties density and Young's modulus, the differential equation of motion for a node in the finite element model is

$$a_n = -\frac{1}{\rho}\left(\frac{\partial P}{\partial x}\right)_n + \frac{E}{\rho}\frac{\left(x_{n+1} + x_{n-1} - 2x_n\right)}{\left(\Delta x_0\right)^2} + \frac{D}{\rho}\frac{\left(v_{n+1} + v_{n-1} - 2v_n\right)}{\left(\Delta x_0\right)^2}. \quad (38)$$

Author disclosure statement

CFB is the only author and has no competing financial interests.

References

1. Rosenfeld JV, McFarlane AC, Bragge P, Armonda RA, Grimes JB, Ling GS (2013). Blast-related traumatic brain injury. Lancet Neurol 12, 882-893.
2. Bauman RA, Ling G, Tong L, Januszkiewicz A, Agoston D, Delanerolle N, Kim Y, Ritzel D, Bell R, Ecklund J, Armonda R, Bandak F, Parks S (2009). An introductory characterization of a combat-casualty-care relevant swine model of closed head injury resulting from exposure to explosive blast. J Neurotrauma 26, 841-860.
3. DePalma RG, Hoffman SW (2018). Combat blast related traumatic brain injury (tbi): Decade of recognition; promise of progress. Behav Brain Res 340, 102-105.
4. Cernak I, Savic J, Ignjatovic D, Jevtic M (1999). Blast injury from explosive munitions. J Trauma 47, 96-103; discussion 103-104.
5. Nakagawa A, Manley GT, Gean AD, Ohtani K, Armonda R, Tsukamoto A, Yamamoto H, Takayama K, Tominaga T (2011). Mechanisms of primary blast-induced traumatic brain injury: Insights from shock-wave research. J Neurotrauma 28, 1101-1119.
6. Gupta RK, Przekwas A (2013). Mathematical models of blast-induced tbi: Current status, challenges, and prospects. Front Neurol 4, 59.
7. Svetlov SI, Larner SF, Kirk DR, Atkinson J, Hayes RL, Wang KK (2009). Biomarkers of blast-induced neurotrauma: Profiling molecular and cellular mechanisms of blast brain injury. J Neurotrauma 26, 913-921.
8. Bhattacharjee Y (2008). Neuroscience. Shell shock revisited: Solving the puzzle of blast trauma. Science 319, 406-408.
9. Taber KH, Warden DL, Hurley RA (2006). Blast-related traumatic brain injury: What is known? J Neuropsychiatry Clin Neurosci 18, 141-145.
10. Garman RH, Jenkins LW, Switzer RC, 3rd, Bauman RA, Tong LC, Swauger PV, Parks SA, Ritzel DV, Dixon CE, Clark RS, Bayir H, Kagan V, Jackson EK, Kochanek PM (2011). Blast exposure in rats with body shielding is characterized primarily by diffuse axonal injury. J Neurotrauma 28, 947-959.
11. Wang H, Zhang YP, Cai J, Shields LB, Tuchek CA, Shi R, Li J, Shields CB, Xu XM (2016). A compact blast-induced traumatic brain injury model in mice. J Neuropathol Exp Neurol 75, 183-196.
12. Riedy G, Senseney JS, Liu W, Ollinger J, Sham E, Krapiva P, Patel JB, Smith A, Yeh PH, Graner J, Nathan D, Caban J, French LM, Harper J, Eskay V, Morissette J, Oakes TR (2016). Findings from structural mr imaging in military traumatic brain injury. Radiology 279, 207-215.
13. Mac Donald CL, Johnson AM, Cooper D, Nelson EC, Werner NJ, Shimony JS, Snyder AZ, Raichle ME, Witherow JR, Fang R, Flaherty SF, Brody DL (2011). Detection of blast-related traumatic brain injury in u.S. Military personnel. N Engl J Med 364, 2091-2100.

14. Jorge RE, Acion L, White T, Tordesillas-Gutierrez D, Pierson R, Crespo-Facorro B, Magnotta VA (2012). White matter abnormalities in veterans with mild traumatic brain injury. Am J Psychiatry 169, 1284-1291.
15. Matthews SC, Spadoni AD, Lohr JB, Strigo IA, Simmons AN (2012). Diffusion tensor imaging evidence of white matter disruption associated with loss versus alteration of consciousness in warfighters exposed to combat in operations enduring and iraqi freedom. Psychiatry Res 204, 149-154.
16. Cernak I, Noble-Haeusslein LJ (2010). Traumatic brain injury: An overview of pathobiology with emphasis on military populations. J Cereb Blood Flow Metab 30, 255-266.
17. Jean A, Nyein MK, Zheng JQ, Moore DF, Joannopoulos JD, Radovitzky R (2014). An animal-to-human scaling law for blast-induced traumatic brain injury risk assessment. Proc Natl Acad Sci U S A 111, 15310-15315.
18. Taylor PA, Ludwigsen JS, Ford CC (2014). Investigation of blast-induced traumatic brain injury. Brain Inj 28, 879-895.
19. Scott SG, Belanger HG, Vanderploeg RD, Massengale J, Scholten J (2006). Mechanism-of-injury approach to evaluating patients with blast-related polytrauma. J Am Osteopath Assoc 106, 265-270.
20. Kodama T, Uenohara H, Takayama K (1998). Innovative technology for tissue disruption by explosive-induced shock waves. Ultrasound Med Biol 24, 1459-1466.
21. Moore DF, Jerusalem A, Nyein M, Noels L, Jaffee MS, Radovitzky RA (2009). Computational biology - modeling of primary blast effects on the central nervous system. Neuroimage 47 Suppl 2, T10-20.
22. Zhang J, Pintar FA, Yoganandan N, Gennarelli TA, Son SF (2009). Experimental study of blast-induced traumatic brain injury using a physical head model. Stapp Car Crash J 53, 215-227.
23. Chafi MS, Karami G, Ziejewski M (2010). Biomechanical assessment of brain dynamic responses due to blast pressure waves. Ann Biomed Eng 38, 490-504.
24. Courtney AC, Courtney MW (2009). A thoracic mechanism of mild traumatic brain injury due to blast pressure waves. Med Hypotheses 72, 76-83.
25. Moss WC, King MJ, Blackman EG (2009). Skull flexure from blast waves: A mechanism for brain injury with implications for helmet design. Phys Rev Lett 103, 108702.
26. Kato K, Fujimura M, Nakagawa A, Saito A, Ohki T, Takayama K, Tominaga T (2007). Pressure-dependent effect of shock waves on rat brain: Induction of neuronal apoptosis mediated by a caspase-dependent pathway. J Neurosurg 106, 667-676.
27. Panzer MB, Myers BS, Capehart BP, Bass CR (2012). Development of a finite element model for blast brain injury and the effects of csf cavitation. Ann Biomed Eng 40, 1530-1544.
28. Walls MK, Race N, Zheng L, Vega-Alvarez SM, Acosta G, Park J, Shi R (2016). Structural and biochemical abnormalities in the absence of acute deficits in mild primary blast-induced head trauma. J Neurosurg 124, 675-686.
29. Song S, Race NS, Kim A, Zhang T, Shi R, Ziaie B (2015). A wireless intracranial brain deformation sensing system for blast-induced traumatic brain injury. Sci Rep 5, 16959.
30. Connell S, Gao J, Chen J, Shi R (2011). Novel model to investigate blast injury in the central nervous system. J Neurotrauma 28, 1229-1236.
31. Race N, Lai J, Shi R, Bartlett EL (2017). Differences in postinjury auditory system pathophysiology after mild blast and nonblast acute acoustic trauma. J Neurophysiol 118, 782-799.
32. Garcia-Gonzalez D, Race NS, Voets NL, Jenkins DR, Sotiropoulos SN, Acosta G, Cruz-Haces M, Tang J, Shi R, Jerusalem A (2018). Cognition based btbi mechanistic criteria; a tool for preventive and therapeutic innovations. Sci Rep 8, 10273.
33. Zhang L, Makwana R, Sharma S (2013). Brain response to primary blast wave using validated finite element models of human head and advanced combat helmet. Front Neurol 4, 88.

34. Pudenz RH, Shelden CH (1946). The lucite calvarium-a method for direct observation of the brain. Journal of Neurosurgery 3, 487-505.
35. Gosch HH, Gooding E, Schneider RC (1969). Distortion and displacement of the brain in experimental head injuries. Surg Forum 20, 425-426.
36. Gosch HH, Gooding E, Schneider RC (1970). The lexan calvarium for the study of cerebral responses to acute trauma. J Trauma 10, 370-376.
37. Ommaya AK (1966). Experimental head injury in the monkey. In: Caveness WF, Walker AE, eds. Head injury. J B lippincott Company: Philadelphia, 260-275.
38. Shridharani JK, Wood GW, Panzer MB, Capehart BP, Nyein MK, Radovitzky RA, Bass CR (2012). Porcine head response to blast. Front Neurol 3, 70.
39. Alley MD, Schimizze BR, Son SF (2011). Experimental modeling of explosive blast-related traumatic brain injuries. Neuroimage 54 Suppl 1, S45-54.
40. Taylor PA, Ford CC (2009). Simulation of blast-induced early-time intracranial wave physics leading to traumatic brain injury. J Biomech Eng 131, 061007.
41. Nyein MK, Jason AM, Yu L, Pita CM, Joannopoulos JD, Moore DF, Radovitzky RA (2010). In silico investigation of intracranial blast mitigation with relevance to military traumatic brain injury. Proc Natl Acad Sci U S A 107, 20703-20708.
42. Namas C, Aravind S (2015). Acute pathophysiology of blast injury—from biomechanics to experiments and computations. In: FH K, ed. Brain neurotrauma: Molecular, neuropsychological, and rehabilitation aspects. CRC Press/Taylor & Francis: Boca Raton, Florida.
43. Babbs CF (2005). Brain motion and deformation during closed head injury in the presence of cerebrospinal fluid. Journal of Mechanics in Medicine and Biology 5, 277-306.
44. Ommaya A (1967). Mechanical properties of tissues of the nervous system. Biomechanics 1, 127-139.
45. Pervin F, Chen WW (2009). Dynamic mechanical response of bovine gray matter and white matter brain tissues under compression. J Biomech 42, 731-735.
46. McElhaney JH, Fogle JL, Melvin JW, Haynes RR, Roberts VL, Alem NM (1970). Mechanical properties on cranial bone. J Biomech 3, 495-511.
47. Brekhovskikh L, Goncharov V (1994). Mechanics of continua and wave dynamics. Springer-Verlag: Berlin.
48. Fung YC (1981). Biomechanics : Mechanical properties of living tissues. Springer-Verlag: New York.
49. Inglese M, Makani S, Johnson G, Cohen BA, Silver JA, Gonen O, Grossman RI (2005). Diffuse axonal injury in mild traumatic brain injury: A diffusion tensor imaging study. J Neurosurg 103, 298-303.
50. Long JB, Bentley TL, Wessner KA, Cerone C, Sweeney S, Bauman RA (2009). Blast overpressure in rats: Recreating a battlefield injury in the laboratory. J Neurotrauma 26, 827-840.
51. Peskind ER, Petrie EC, Cross DJ, Pagulayan K, McCraw K, Hoff D, Hart K, Yu CE, Raskind MA, Cook DG, Minoshima S (2011). Cerebrocerebellar hypometabolism associated with repetitive blast exposure mild traumatic brain injury in 12 iraq war veterans with persistent post-concussive symptoms. Neuroimage 54 Suppl 1, S76-82.